



A parametric study of damage initiation and propagation in EB-PVD thermal barrier coatings

Himanshu Bhatnagar, Somnath Ghosh *, Mark E. Walter

Department of Mechanical Engineering, The Ohio State University, 201 West 19th Avenue, Columbus, OH 43210, USA

ARTICLE INFO

Article history:

Received 22 February 2009

Received in revised form 13 September 2009

Keywords:

Thermal barrier coatings

Hysteretic cohesive zone model

Crack initiation and propagation

Finite element method

Cyclic thermal loading

ABSTRACT

In this paper, finite element models are used to investigate catastrophic failure of thermal barrier coatings (TBCs) due to delaminations along susceptible interface between thermally grown oxide (TGO) and the ceramic top coat. The top coat crack initiation and propagation is investigated using a thermo-elastic finite element model with bond coat creep. Cracks are assumed to initiate when the maximum principal stress exceeds rupture stress of the top coat. A sensitivity analysis estimates the contribution of geometric and material parameters. Subsequently, crack propagation simulations using a hysteretic cohesive zone model are performed for parametric combinations which initiate top coat cracks. A parametric relationship is established for assessing crack initiation in terms of geometric and material parameters of the TBC that helps identify the fail-safe design space for TBC. The finite element predictions are also compared to the experimental observations of failure.

© 2009 Elsevier Ltd. All rights reserved.

1. Introduction

The state-of-the-art electron beam physical vapor deposition (EB-PVD) thermal barrier coatings (TBCs) are used in gas turbine engines to protect components from high temperature gases and severe transient thermal loading. As shown in the SEM micrograph of Fig. 1, a conventional TBC consists of three layers deposited on a super-alloy substrate. The first layer is a 50–100 μm thick bond coat that provides oxidation protection, while the second is a 100–120 μm thick top coat for providing thermal insulation. The top coat is structured to be strain tolerant to avoid cracking and subsequent delamination; this is achieved by incorporating micro-cracks or aligned porosity in the material (Wright and Evans, 1999). Typically, due to its low, temperature-insensitive thermal conductivity (Wright and Evans, 1999), yttria-stabilized zirconia is the material of choice for the top coat. The top coat is transparent to oxygen, and thus a third layer, the thermally grown oxide (TGO) forms as the bond coat oxidizes. Due to TGO growth and the creep deformation of the bond coat,

the morphology of the TGO interfaces with adjoining layers continue to evolve during the life of the TBC (Spitsberg et al., 2005). As shown in Fig. 1, the SEM images of the TBC microstructure reveal that the TGO interfaces may be planar or wavy.

Experimental observations by Wang and Evans (1998) have confirmed that in the absence of bond coat creep, delamination at the TGO and bond coat interface leads to buckling instability and failure in TBCs. The onset of failure along TGO and bond coat interface may be viewed as a competition between strain energy driven interfacial crack growth mechanism and buckling induced instability and delamination. Recently, Bhatnagar et al. (2005) investigated the characteristics of the failure modes along the TGO and bond coat interface (e.g. buckling instability and strain energy driven delamination propagation) using thermo-elastic finite element models. The solution of a linear elastic eigen-value problem determines the onset of the buckling instability with a pre-existing delamination between bond coat and the TGO. The virtual crack extension method predicts strain energy release rate driven interfacial delamination at wavy interfaces. An extensive sensitivity analysis identifies the critical design parameters affecting the onset of buckling and extension of interfacial

* Corresponding author.

E-mail address: ghosh.5@osu.edu (S. Ghosh).

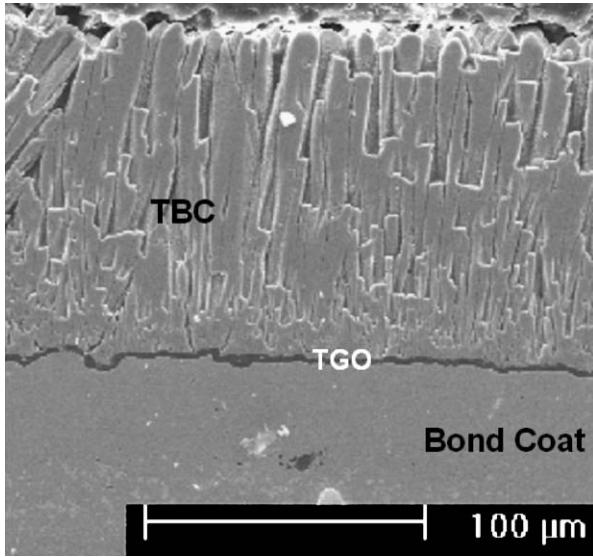


Fig. 1. An SEM image of the TBC microstructure consisting of the top coat, the thermally grown oxide layer, the bond coat and the super-alloy substrate (Kim, 2005).

delamination. The sensitivity analysis is used to derive parametric equation for buckling instability and delamination extension summarized in Eqs. (1) and (2), respectively. For any given configuration, material and load condition, the critical stress can therefore be determined for each mechanism. A comparative analysis using these equations can determine optimal configurations for the TBC system from a fail-safe point of view.

$$\sigma_{TGO}^{b3} = \sigma_{TGO}^{b2} + \left(\frac{h}{R}\right)^{-0.45} \left(1 - e^{-(C_1 \frac{h}{R})}\right) \left(C_2 \frac{E_{TC}^2}{E^*} + C_3 E_{TC}\right) \quad \forall 0.25 \leq \left(\frac{h}{R}\right) \leq 1.0 \quad (1)$$

where σ_{TGO}^{b2} is the critical TGO stress for two layer TBCs, $E^* = 1$ GPa (necessary for dimensional consistency) and C_1 , C_2 and C_3 are constants determined to be: $C_1 = 1.115$, $C_2 = -1.33E-3$ and $C_3 = 0.746$.

$$\sigma_{TGO}^c = \left(\frac{G^c}{(\tan^{-1} \psi)^{C_1} \left(C_2 t e^{-C_3 \frac{t}{t_0}} - C_4 \frac{h^2}{h_0} + C_5 h \right) \left(1 - e^{-C_6 \frac{R}{R_0}} \right) \zeta} \right)^{0.5} \quad (2)$$

where $\psi = \left(\frac{2\pi A + 3h}{W}\right)$, $\zeta = \left(C_7 \frac{1}{E_{TGO}} + C_8 \frac{(\alpha_{TC} - \alpha_{BC})^2 E_{TC}}{(\alpha_{TGO} - \alpha_{BC})^2 E_{TGO}^2} e^{-C_9 \frac{E_{TC}}{E^*}}\right)$, $t_0 = 1 \mu\text{m}$, $h_0 = 1 \mu\text{m}$, $R_0 = 1 \mu\text{m}$, $E^* = 1$ GPa, $(\alpha_{\text{layer}} - \alpha_{BC})$ is the CTE mismatch of the layers and $C_1 - C_9$ are constants derived to be: $C_1 = 3.62$, $C_2 = 2.02 \times 10^3$, $C_3 = 0.92$, $C_4 = 17.83$, $C_5 = 427.97$, $C_6 = 0.14$, $C_7 = 1.10$, $C_8 = 111.25$ and $C_9 = 0.12$.

In addition, a numerical exercise (Bhatnagar et al., 2005) has demonstrated that the buckling instability is the leading failure mechanism at flat interfaces or at the locations of minimum cross-section in a wavy interface. However, in the vicinity of waviness, crack extension becomes a dominant mode of failure.

There is experimental evidence that with significant bond coat creep, damage initiates within the top coat that leads to delamination of the top coat and TGO interface (Karlsson et al., 2002, 2003; Xu et al., 2003a,b). Damage within the top coat is driven primarily by the stresses developed due to the coefficient of thermal expansion (CTE) mismatch between the different layers during thermal loading, as well as by creep deformation of the bond coat. Notable amongst the factors which contribute to damage initiation and propagation are thermo-mechanical material properties and morphological features of interfaces and constituent layers.

There exists a significant body of work characterizing the growth of undulations under cyclic loading (Karlsson et al., 2002, 2003; Xu et al., 2003a,b). A number of these investigations also consider the top coat damage (Karlsson et al., 2002, 2003), but the relationship between damage and geometric and material factors has not been addressed in detail. Xu et al. (2003a,b) have demonstrated the variation in energy release rate as the crack propagates within the top coat for crack paths that were selected *a priori*.

The paper is organized as follows: Section 2 explains the TBC computational model and Sections 3 and 4 develop parametric understanding of top coat crack initiation and propagation responsible for eventual delamination of TGO and top coat interface. A parametric relationship for the maximum principal stress with material and geometric parameters is developed to predict crack initiation. Subsequently, crack propagation and the interfacial delamination are investigated for all parametric combinations resulting in cracks initiating away from the interface. As a final step, the crack trajectory predicted by finite element simulation is compared with a top coat cracking observed in a real TBC microstructure.

2. Finite element models of TBCs

A finite element model is developed to investigate delamination of the TGO and top coat interface. The model features bond coat creep and top coat damage evolution, which is characterized by crack initiation and crack propagation phases. To characterize both phases, the following two studies are performed: (a) determination of probable crack initiation and (b) subsequent crack propagation study assuming a finite crack at the initiation locations.

For the first study, a mode I crack initiation criterion similar to Anderson (1995) is employed where damage appears as a finite crack oriented normal to principal direction and when the maximum of first principal stress ($S1^{\text{max}}$) exceeds rupture stress (σ_{rupture}):

$$S1^{\text{max}} \geq \sigma_{\text{rupture}} \quad (3)$$

This criterion enables identification of safer TBC designs through a sensitivity analysis to determine the relationship between $S1^{\text{max}}$ and the various geometric and material parameters. The parameters considered for this study include: (a) top coat modulus (E_{TC}), (b) TGO modulus (E_{TGO}), (c) TGO thickness (h), (d) amplitude (A) and wavelength (W) of the undulation, and (e) thermal cycle parameters including peak temperature and heating, holding, and cool-

ing time. Since the resulting crack is oriented normal to the principal direction, the orientation of the principal axis is recorded to introduce properly oriented nascent cracks.

The subsequent crack propagation study simulates crack propagation by inserting a hysteretic cohesive zone between continuum elements of the finite element mesh. The evolution of the crack path is determined by selecting the direction of maximum cohesive energy as proposed in Li and Ghosh (2006a,b). This eliminates the mesh-dependent prediction of crack path even with a structured mesh (Li and Ghosh, 2006a,b).

Various aspects of this finite element model of the TBC are summarized in the following subsections.

2.1. Material models

The bond coat material of choice for TBCs is an inter-metallic platinum modified nickel aluminide with a CTE similar to that of the substrate material. In this study, a thermally activated creep material model for the bond coat proposed in Pan et al. (2003) is employed. The creep model in Pan et al. (2003) is based on micro-tensile test results performed on bond coats extracted from actual TBC systems and are deemed accurate. The strain rate–stress law in this creep model is expressed as

$$\begin{aligned} \dot{\epsilon}_{\text{creep}} &= 7.5 \times 10^{20} \left(\frac{\sigma}{E}\right)^{2.7} \exp\left(\frac{-340 \text{ kJ/mol}}{RT}\right) & T < 800^\circ\text{C} \\ \dot{\epsilon}_{\text{creep}} &= 9.1 \times 10^{27} \left(\frac{\sigma}{E}\right)^4 \exp\left(\frac{-400 \text{ kJ/mol}}{RT}\right) & T > 800^\circ\text{C} \end{aligned} \quad (4)$$

where $\dot{\epsilon}_{\text{creep}}$ is the equivalent creep strain rate, σ is the equivalent deviatoric stress, R is the gas constant, and T is the absolute temperature. The bond coat material model is implemented as a user subroutine in the ABAQUS (Abaqus, 2005) finite element package.

Advanced TBCs typically have nickel based super-alloy substrates with high strength and stiffness at elevated temperatures. Thus the substrate is treated as an isotropic, elastic material. The top coat and TGO are idealized as an isotropic, elastic material with no pre-existing flaws. Although the columnar structure of the top coat suggests that it will be more compliant under tension than under compression, CTE mismatches between the top coat and substrate would prevent in-plane tension. With little in-plane tension, effects of the columnar microstructure should not be significant. The rupture stress for the top coat is assumed to be same as homogeneous yttria-stabilized zirconia reported in Adams et al. (1997). The material property values for each of the TBC layers are same as those reported in Table 1; values were obtained from Adams et al. (1997), Cheng et al. (1998) and Evans et al. (2001).

2.2. Geometric model and finite element mesh

A finite element model of the TBC system including the substrate, bond coat, TGO, and top coat is shown in Fig. 2. 2D plane strain representations of the TBC system are selected as undulations are assumed to run through the sam-

Table 1

Material properties of components of the TBC system as obtained from Adams et al. (1997), Cheng et al. (1998) and Evans et al. (2001).

Property	Substrate	TGO	TBC
Poisson's ratio	0.31–0.35	0.23–0.25	0.10–0.12
Elastic modulus (GPa)	120–220	320–400	100–220
Thermal expansion coefficient ($10^{-6}/^\circ\text{C}$)	14.8–18.0	4.0–8.0	6.0–12.2
Rupture stress (MPa)	–	–	287

ple thickness. The TBC morphology is assumed to be symmetric about the vertical plane and only the half geometry is modeled. In this study, only sinusoidal undulations penetrating into the bond coat are considered.

A $150 \times 1100 \mu\text{m}$ section of TBC system is modeled with a graded mesh of four-noded elements which are identified as CPE4(QUAD2D) in the ABAQUS element library (Abaqus, 2005). The resulting model consist of more than 11,000 elements and 12,000 nodes, and exhibits less than 0.5% error in the strain energy when compared to a more refined mesh. As shown in Fig. 2b, mesh in the vicinity of the TGO undulation is refined and becomes coarse away from the region of interest.

2.3. Boundary conditions

The TBC system model is subjected to a cyclic thermal load through variation of a uniformly applied temperature from 1000°C to room temperature of 30°C . Each nominal temperature cycle includes 10 min of heating and a 10 min hold at peak temperature and 10 min of cooling. The top surface of the TBC is assumed to be free of any mechanical constraints or loads. Symmetry boundary conditions are applied at the left edge, roller supports are applied at the lower horizontal boundary; and radial periodic boundary conditions are applied at the right edge of the models. These boundary conditions are shown pictorially in Fig. 2b.

2.4. Irreversible hysteretic mixed-mode cohesive zone model

Due to the cyclic nature of the thermal loading, TBCs may incur significant fatigue damage within the top coat leading to crack coalescence and failure. The hysteretic cohesive models proposed by Nguyen et al. (2001) and Maiti and Geubelle (2005) and extended for mixed-mode application by Bhatnagar et al. (2007) will be employed for this investigation. This hysteretic cohesive model reduces to an irreversible bi-linear, rate-independent cohesive law under monotonic loading (Maiti and Geubelle, 2005; Swaminathan et al., 2006).

The bi-linear cohesive model is discussed in detail elsewhere, e.g. (Raghavan and Ghosh, 2005; Swaminathan et al., 2006) and is summarized by the following traction-separation law:

$$T = \begin{cases} \frac{\sigma_{\text{max}}}{\delta_c} \delta & \text{if } \delta < \delta_c \text{ (hardening region)} \\ \frac{\sigma_{\text{max}}}{\delta_c - \delta_e} (\delta - \delta_e) & \text{if } \delta_c < \delta < \delta_e \text{ (softening region)} \\ 0 & \text{if } \delta > \delta_e \text{ (completely debonded)} \end{cases} \quad (5)$$

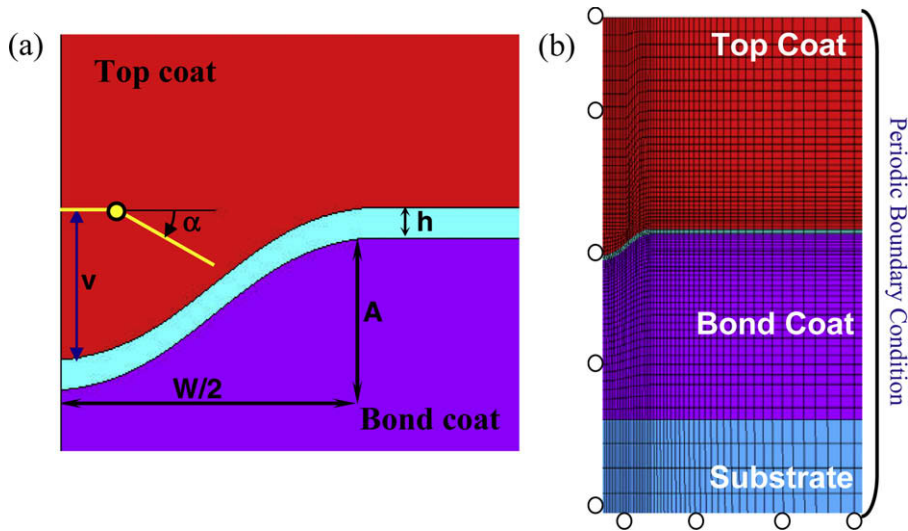


Fig. 2. Schematic diagrams showing (a) geometric and dimensional parameters (b) finite element model (not to scale) of the TBC system with boundary conditions.

The effective separation and effective traction are defined as $\delta = \sqrt{\delta_n^2 + \beta^2 \delta_t^2}$ and $T = \sqrt{T_n^2 + \beta^{-2} T_t^2}$, respectively, where δ_n and T_n are the normal separation and traction, δ_t and T_t are the tangential separation and traction and β is an empirical factor. As shown in Fig. 3 as the effective separation increases, the effective traction across the elements linearly increases to a maximum value (σ_{max}) at δ_c , and then decreases for further increase in separation. This increase in traction is known as hardening and is elastic.

The subsequent decrease is known as softening. Any further unload/reload prior to reaching the maximum separation of δ_e is carried out with lower stiffness. After exceeding δ_c , the element has zero stiffness.

To account for dissipative mechanisms in the fracture process zone ahead of the crack tip, a hysteretic model incurs fatigue damage only during reloading. During reloading the stiffness of the cohesive element is assumed to decay according to the stiffness degradation given below in Eq. (6) and again shown in Fig. 3. The rate of stiffness de-

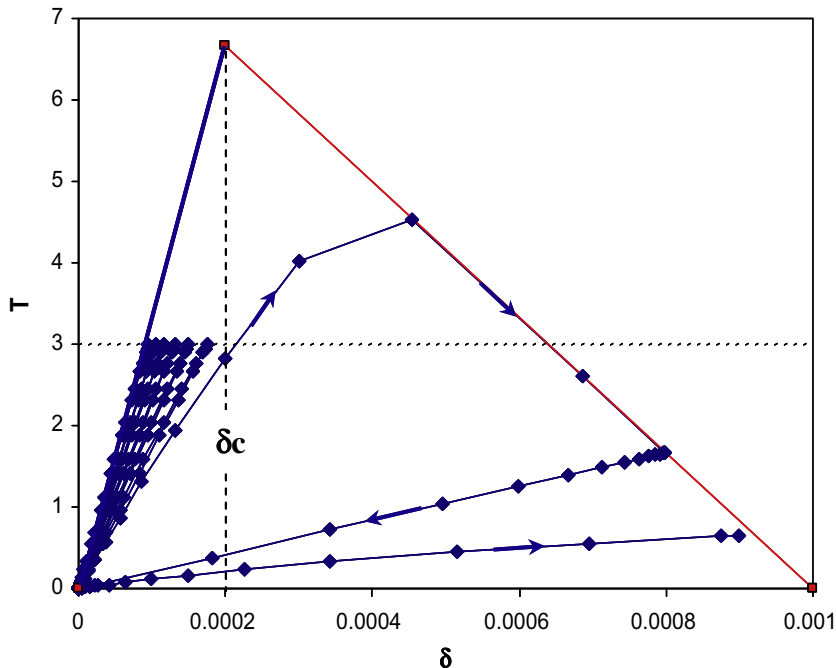


Fig. 3. A plot showing the hysteretic cohesive zone element response with cyclic loading to eventual failure when $\delta = \delta_e = 0.001$.

cay is controlled by the introduction of an additional parameter δ_f .

$$\dot{K}_{nn} = \begin{cases} -K_{nn} \frac{\dot{\delta}_n}{\delta_f} & \text{if } \dot{\delta}_n > 0 \\ 0 & \text{if } \dot{\delta}_n \leq 0 \end{cases} \quad (6)$$

$$\dot{K}_{tt} = \begin{cases} -K_{tt} \frac{\dot{\delta}_t}{\delta_f} & \text{if } \dot{\delta}_t > 0 \\ 0 & \text{if } \dot{\delta}_t \leq 0 \end{cases}$$

These incremental stiffness equations are integrated to calculate the stiffness at the $(p+1)$ th step in terms of the stiffness of the p th load step and increment in displacement jump. The resulting normal and tangential stiffness are:

$$K_{nn}^{p+1} = K_{nn}^p e^{-\frac{\Delta\delta_n}{\delta_f}} \quad \text{and} \quad K_{tt}^{p+1} = K_{tt}^p e^{-\frac{\Delta\delta_t}{\delta_f}} \quad (7)$$

where $\Delta\delta_n = \delta_n^{p+1} - \delta_n^p$ and $\Delta\delta_t = \delta_t^{p+1} - \delta_t^p$.

The hysteretic response of the cohesive model remains within the envelope of the bi-linear model, and when the reloading curve intersects the softening curve it follows the curve for as long as the loading process continues. During such periods the element accrues only monotonic damage without any fatigue damage. From the above formulation, it can be seen that five cohesive zone parameters namely, σ_{\max} , δ_c , δ_e , δ_f , and β define the hysteretic cohesive model response.

This hysteretic cohesive model is implemented as a four-noded cohesive element within an ABAQUS User defined Element (UEL) subroutine (Abaqus, 2005). These elements are compatible with the regular, continuum ABAQUS QUAD2D elements. The element is comprised of two cohesive surfaces with two nodes each. In the initial, unloaded state, the nodes of the two surfaces share the same coordinates. With the application of external load, the surfaces move and separate from one another as the adjacent solid elements deform. The relative normal and tangential tractions for the 2D cohesive elements are calculated at the element integration points according to the traction-separation law defined by Eq. (5). The element has two integration points corresponding to those of the QUAD2D element. Fig. 2 shows a TBC finite element model with cohesive elements along a representative crack path.

2.5. Incremental direction of crack propagation

The crack trajectory cannot be determined *a priori* as it depends on the local drivers at the crack tip. Since the crack is restricted to follow the trajectory defined by the cohesive zone elements, it is imperative to evaluate the direction of crack propagation at each increment of loading. In the present work direction is determined using the maximum cohesive energy criterion proposed by Li and Ghosh 2006(a,b). This criterion postulates that the crack will propagate in the direction that maximizes the cohesive energy. From the definition of the J -integral, a relation between the cohesive energy ϕ for complete decohesion and the critical energy release rate G_c has been established by Ortiz and Pandolfi (1999) as:

$$G_c = J = \int_0^R T \frac{\partial \delta}{\partial x} dx = \int_0^{\delta_e} T d\delta = \phi \quad (8)$$

where R is the length of the cohesive zone. Consequently, for a given crack tip state of stress, the crack growth direction is estimated as that along which G_c or equivalently the cohesive energy ϕ is maximized. The cohesive energy ϕ_A at the crack tip A along any direction α can be expressed for an arbitrary effective separation $\delta(\alpha)$ as:

$$\phi_A(\alpha) = \left(\int_0^{\delta} T(\alpha) d\delta \right)_A = \left(\int_0^t T(\alpha) \frac{\partial \delta}{\partial t} dt \right)_A \quad (9)$$

where $T(\alpha) = \sqrt{(T_n^{\text{coh}})^2 + \beta^{-2} (T_t^{\text{coh}})^2}$ is the magnitude of the effective cohesive traction. The corresponding unit normal 'n' and tangential 't' vectors along the direction α are expressed as:

$$n = -\sin \alpha i + \cos \alpha j \quad \text{and} \quad t = \cos \alpha i + \sin \alpha j \quad (10)$$

The normal and tangential components of the cohesive traction force at an angle α are then deduced as:

$$\begin{Bmatrix} T_n^{\text{coh}} \\ T_t^{\text{coh}} \end{Bmatrix} = \begin{bmatrix} n_x & n_y \\ t_x & t_y \end{bmatrix} \begin{Bmatrix} \sigma_{xx} n_x + \sigma_{xy} n_y \\ \sigma_{xy} n_x + \sigma_{yy} n_y \end{Bmatrix}$$

$$= \begin{Bmatrix} \sigma_{xx} \sin^2 \alpha + \sigma_{xy} \sin 2\alpha + \sigma_{yy} \cos^2 \alpha \\ -\frac{1}{2} \sigma_{xx} \sin 2\alpha + \sigma_{xy} \cos 2\alpha + \frac{1}{2} \sigma_{yy} \sin 2\alpha \end{Bmatrix} \quad (11)$$

and hence the effective cohesive traction for direction α is:

$$T(\alpha) = \sqrt{\left(\sigma_{xx} \sin^2 \alpha - \sigma_{xy} \sin 2\alpha + \sigma_{yy} \cos^2 \alpha \right)^2 + \beta^{-2} \left(-\frac{1}{2} \sigma_{xx} \sin 2\alpha + \sigma_{xy} \cos 2\alpha + \frac{1}{2} \sigma_{yy} \sin 2\alpha \right)^2} \quad (12)$$

$\phi_A(\alpha)$ is evaluated by inserting Eqs. (12) into (9) and maxima is obtained using the extremum criteria in Eq. (13). Thus, the resulting direction of crack propagation α_0 is reported in Eq. (14).

$$\frac{\partial \phi_A(\alpha)}{\partial \alpha} = 0 \quad \text{and} \quad \frac{\partial^2 \phi_A(\alpha)}{\partial \alpha^2} < 0. \quad (13)$$

$$\alpha_0 = \sin^{-1} \left(\frac{\sigma_{yy} - \sigma_{xx} \pm \sqrt{(\sigma_{xx} - \sigma_{yy})^2 + 4\sigma_{xy}^2}}{\sqrt{\left(\sigma_{yy} - \sigma_{xx} \pm \sqrt{(\sigma_{xx} - \sigma_{yy})^2 + 4\sigma_{xy}^2} \right)^2 + 4\sigma_{xy}^2}} \right). \quad (14)$$

Any change in crack trajectory is achieved by generating a new mesh incorporating an updated crack path laced with cohesive elements. To reduce the computational expense associated with this process, the crack trajectory is updated when there are tendencies for significant directional change.

2.6. Selection of cohesive zone parameters

A rigorous methodology is followed for the selection of five cohesive zone parameters namely, σ_{\max} , δ_c , δ_e , δ_f , and β defining the hysteretic cohesive zone response. First, the peak stress σ_{\max} is set equal to the rupture stress of the top coat material, thus simulating the onset of damage. Next, selection of δ_c determines the hardening stiffness

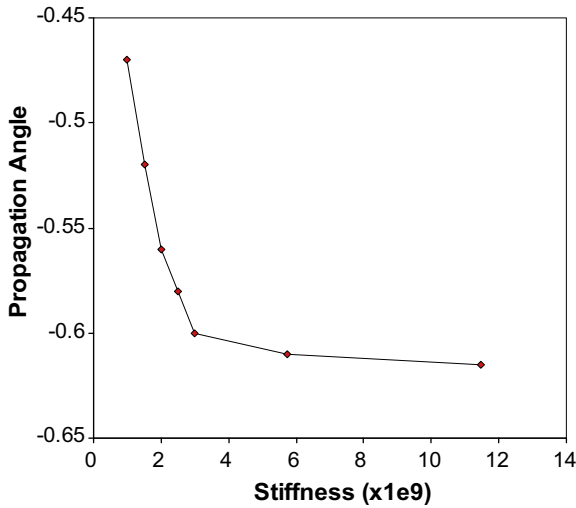


Fig. 4. Plot showing the convergence of crack propagation angle with increasing cohesive stiffness (σ_{\max}/δ_e).

(σ_{\max}/δ_c) of the cohesive zone and requires sensitivity study. Fig. 4 summarizing the sensitivity study and shows that the crack propagation angle α_0 computed by Eq. (14) monotonically converges to a stabilized value with increasing hardening stiffness. For hardening stiffness above 6e9 MPa/ μm the variation in α_0 becomes less than 1% and convergence is assumed. Hence, δ_c is computed using this stiffness along with the selected σ_{\max} . Furthermore, δ_e is computed by equating the cohesive energy to fracture toughness of the material as demonstrated in Eq. (8). Finally, the fatigue damage parameter δ_f is chosen to be $5\delta_e$.

3. Parametric modeling of crack initiation in the top coat

Simulations conducted with the computational models discussed in Section 4.2 are used to derive a functional form for the maximum principal stress ($S1^{\max}$) in terms of important geometrical and material parameters in the TBC system. Sensitivity analyses of these drivers are conducted with respect to various parameters and the results are utilized in the determination of the functional dependence. Although, finite element simulations show that location of maximum principal stress is variable only $S1^{\max}$ magnitude variation is considered for development of the parametric relation. Candidate parameters considered in the sensitivity analysis are: (i) h , thickness of the TGO; (ii) A , amplitude of the sinusoidal undulation; (iii) W , wavelength of the undulation; (iv) t , thickness of the top coat; (v) E_{TGO} , modulus of the TGO; and (vi) E_{TC} , modulus of the top coat. Definitions of the geometric parameters are pictorially given in Fig. 2a. The parametric space is defined by parameter ranges given in Table 2.

For sensitivity analyses, a parametric matrix covering all possible combinations of parameters and their values is generated. To limit the number of analyses few discrete values are selected for each parameter to represent its

Table 2

Range of variation of parameters from experimental observations reported in Choi et al. (1999), Evans et al. (2001), Gell et al. (1999), Mumm et al. (2001), Spitsberg et al. (2005) and Tolpygo and Clarke (2000).

Parameter	Range of variation
TGO thickness (h)	2–6 μm
Undulation amplitude (A)	5–50 μm
Undulation wavelength (W)	10–160 μm
TC thermal expansion (a_{TC})	$6\text{--}12 \times 10^{-6}$
TGO thermal expansion (a_{TGO})	$4\text{--}8 \times 10^{-6}$
Top coat modulus (E_{TC})	100–220 GPa
TGO modulus (E_{TGO})	320–400 GPa

range. The simulations revealed that the magnitude and location of $S1^{\max}$ in the top coat is sensitive to several parameters. A representative set of the sensitivity analyses results for $S1^{\max}$ magnitude are summarized in Fig. 5a and b, where the normalized $S1^{\max}$ is plotted as a function of the normalized geometric and material parameters,

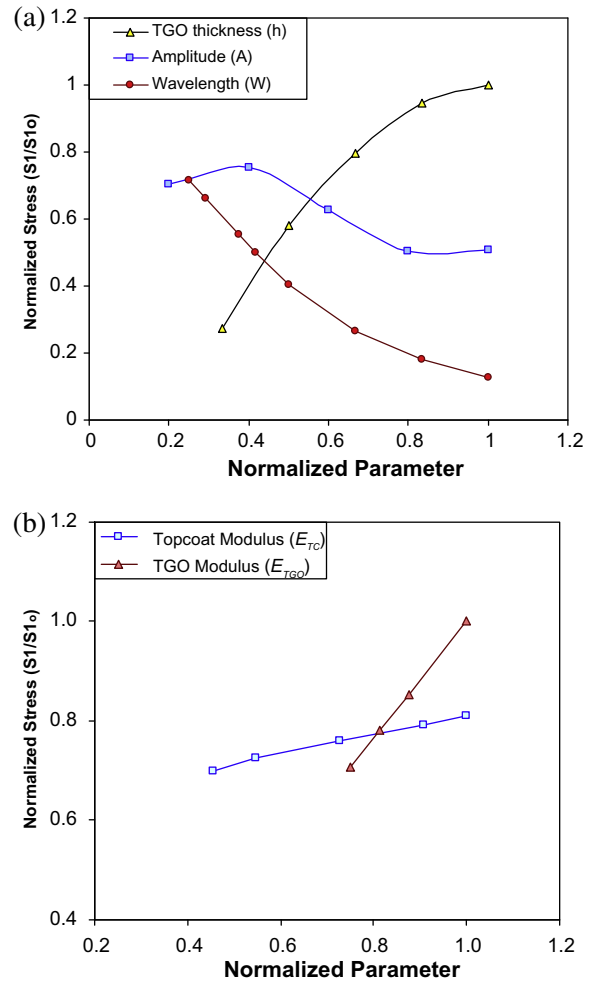


Fig. 5. Plots showing top coat principal stress sensitivity to (a) geometric parameters (normalizing values of $h_{\max} = 6 \mu\text{m}$, $A_{\max} = 25 \mu\text{m}$, $W_{\max} = 120 \mu\text{m}$, and $S1_0 = 604 \text{ MPa}$), (b) material parameters (normalizing values of $E_{\text{TGO}}^{\max} = 400 \text{ GPa}$, $E_{\text{TC}}^{\max} = 220 \text{ GPa}$ and $S1_0 = 410.89 \text{ MPa}$).

respectively. The $S1^{\max}$ for each plot is normalized with $S1_0^{\max}$, the maximum amongst all reported results in that plot. Each parameter is normalized with its maximum value in Table 2. Beyond the nominal values ($b = 60 \mu\text{m}$ and $t = 100 \mu\text{m}$) $S1^{\max}$ is found to be insensitive to any increase in the top coat thickness t or the bond coat thickness b . Fig. 5a shows that principal stress decreases exponentially with increasing undulation wavelength W and asymptotically approaches zero. This is confirmed by the fact that an undulation with infinite wavelength corresponds to a flat interface for which the $S1^{\max}$ principal stress is zero. For increasing amplitude A , there is first an increase in the principle stress and then exponential decay. Finally, the principal stress increases monotonically with the TGO thickness h .

Fig. 5b shows that $S1^{\max}$ linearly increases with increasing top coat modulus. The response is similar for increasing

TGO modulus but with a much steeper slope. The graph also elucidates that a minor reduction in TGO modulus will prevent top coat crack initiation as $S1^{\max}$ decreases below rupture stress.

3.1. Parametric representation for crack initiation in the top coat

From the summary of results in Fig. 5, the critical parameters selected are the top coat modulus E_{TC} , TGO thickness h and modulus E_{TGO} , undulation wavelength W and amplitude A . Based on their influence on $S1^{\max}$, the geometric parameters are re-classified into three basic non-dimensional groups h/h_0 , W/A and A/A_0 and the sensitivity study results are used to establish functional relations. The material parameters E_{TC} and E_{TGO} are assigned a linear function based on the linear response shown in

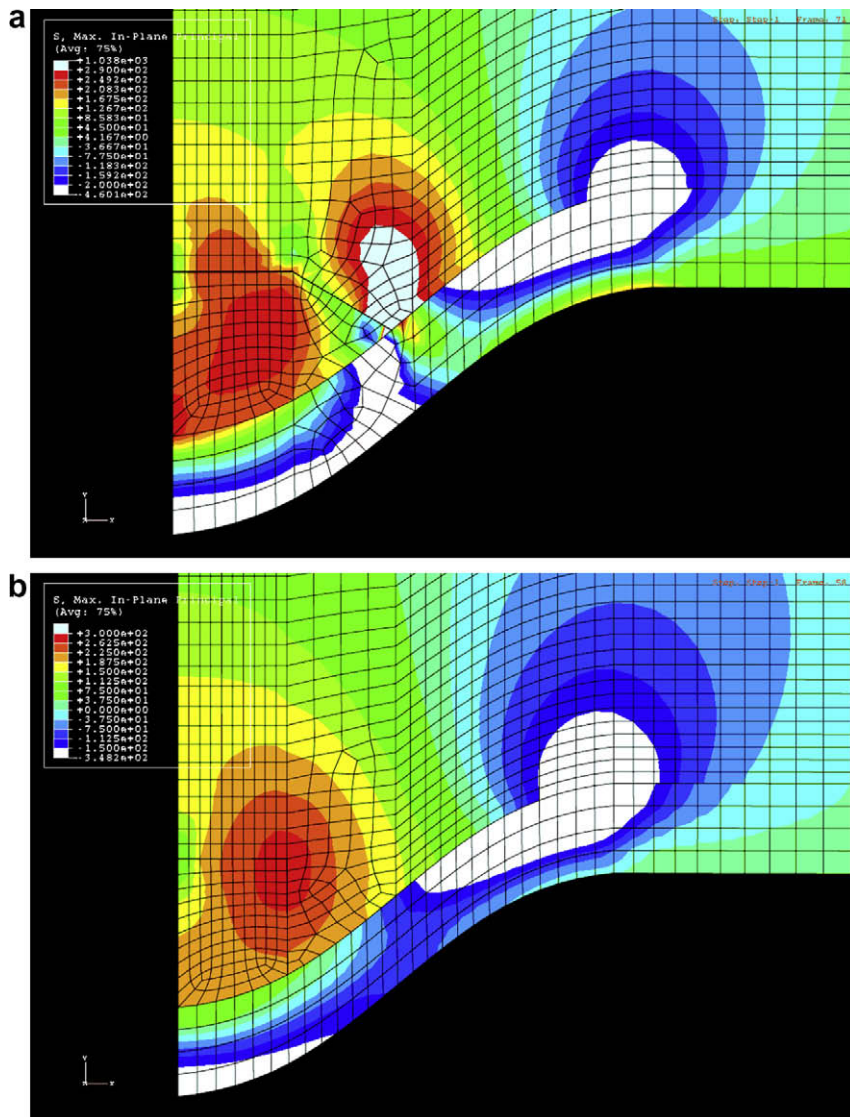


Fig. 6. Plots of principal stress contours showing crack arrest when prescribed path deviates by (a) 30° and (b) 90° from that predicted by Eq. (14).

Fig. 5b. All the individual functions are subsequently combined to derive the following functional dependence for the maximum principal stress:

$$S1_{\max} = c_1 \left(1 + c_2 \frac{h}{h_0} e^{-\frac{W}{4A}} \right) \left(\frac{(A/A_0)}{1 + (A/A_0)^2} \right) \left(1 + c_3 \frac{E_{TC}}{E^*} \right) E_{TGO} \tag{15}$$

where $A_0 = 1 \mu\text{m}$, $h_0 = 1 \mu\text{m}$, $E^* = 100 \text{ GPa}$ and $c_1 - c_3$ are constants. The constants in Eq. (15) are evaluated using a least squares based best fit analysis of all FEM results with a tolerance of 15%. For stress and moduli expressed in GPa and lengths in μm , the constants are derived to be: $c_1 = 0.8124$, $c_2 = 5.000$ and $c_3 = 0.1320$.

4. Parametric investigation of top coat crack propagation

The parametric relation for $S1^{\max}$ established in Eq. (15) predicts the crack initiation within the top coat, however, its severity on failure is determined by its location. The cracks initiating at the interface would lead to large scale delamination and are considered critical, whereas the cracks initiating away from the interface are critical only if they propagate to the TGO-top coat interface. Hence, subsequent to crack initiation sensitivity analysis, crack propagation simulations are performed for 25 unique parametric combinations that resulted in cracks initiating away from the interface. Due to the evolutionary nature of the crack trajectory these simulations are performed iteratively with finite element mesh regeneration for each significant deviation in crack path. Initially, a linear crack path oriented normal to the principal axis is prescribed and laced with hysteretic cohesive elements. The optimal crack increment direction is evaluated using Eq. (14) for each increment in crack length and when it deviates significantly from prescribed path the simulation is terminated. Subsequently, the crack path is updated linearly along the incremental direction and finite element mesh is regenerated for the updated crack path. In addition to monitoring the incremental direction for crack propagation, the rate of crack propagation is also monitored for each increment.

4.1. Validation of top coat crack propagation direction

Prior to performing the crack propagation investigation, a sensitivity study is conducted to estimate the effect of variation in crack propagation direction on the propagation rate. The sensitivity analysis is performed using a representative parametric combination with $A = 10 \mu\text{m}$, $W = 40 \mu\text{m}$, $h = 4 \mu\text{m}$, $E_{TGO} = 400 \text{ GPa}$ and $E_{TC} = 200 \text{ GPa}$. For this combination of parameters, crack initiates perpendicular to the symmetry axis at a normal distance of $6.35 \mu\text{m}$ from the interface. Using the crack propagation angle in Eq. (14) crack should deviate by 1° from horizontal after propagating $5 \mu\text{m}$ to location **P** shown in Fig. 2a. To evaluate the effect of incremental direction on propagation rate, in addition to the 1° determined by Eq. (14), three distinct propagation angles 90° , 60° and 30° are prescribed at the crack tip. The results of subsequent crack propagation analyses show that the crack remains arrested at **P** for the propagation angles 90° ,

60° and 30° but propagates at an accelerating rate along the 1° direction. The results of crack propagation analyses for 30° and 90° are shown in Fig. 6a and b.

This study demonstrates a strong influence of incremental direction on propagation rate and also confirms that the propagation direction evaluated by Eq. (14) is most favorable for crack propagation.

4.2. Top coat crack propagation results

Crack propagation simulations show that the crack trajectories do not undergo significant deviations and remain oriented along the initially prescribed linear path. Amongst all simulations the maximum deviation in crack path until the interface is observed to be 4° . Fig. 7 summarizes the results with a representative parametric combination of $A = 10 \mu\text{m}$, $W = 40 \mu\text{m}$, $h = 4 \mu\text{m}$ that initiates a crack at a perpendicular distances of $6.01 \mu\text{m}$ from the interfacial

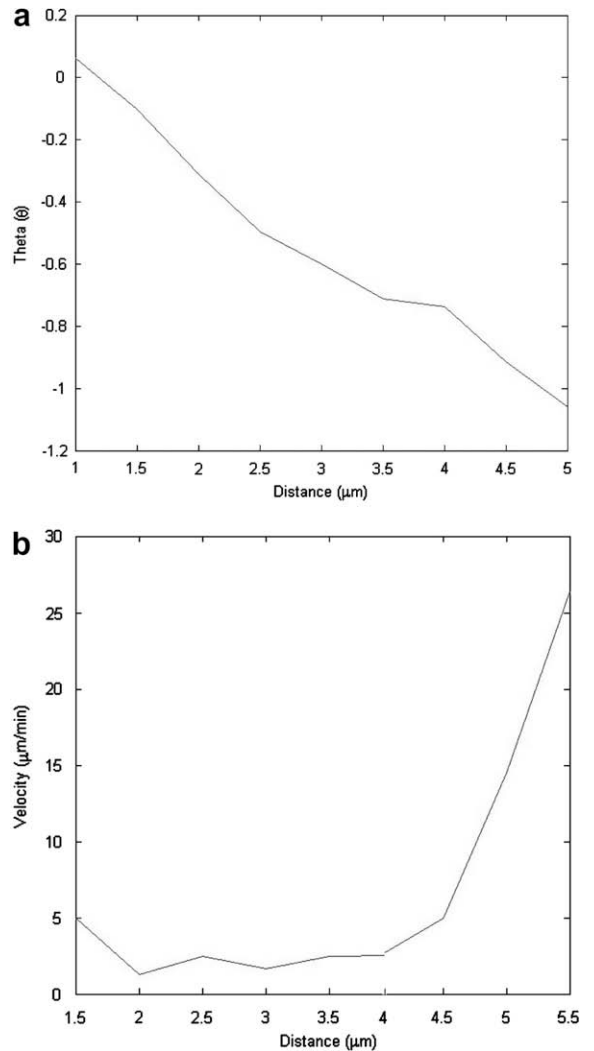


Fig. 7. Plots showing the variation in (a) incremental crack propagation direction and (b) crack propagation rate as the crack propagates along an initially assigned path towards the interface.

trough. Fig. 7a shows the variation in incremental propagation direction as the crack propagates towards the interface along the initially prescribed linear crack path. It should be noted that incremental directions are negative, thus indicating the crack is deviating towards the undulation. Fig. 7b illustrates the corresponding rate of propagation measured as the crack extension per minute during the thermal cycle. The propagation rates increase as crack tip advances towards the interface and achieves peak values in the vicinity of the interface. There is significant difference in the initial rates of propagation between different parametric combinations, however, the propagation rate monotonically increases as crack tip approaches the interface and, for all cases achieves very high values at the interface.

These simulations conclude that the parametric combinations that initiate cracks away from the interface also assist in the crack propagation towards the TGO and top coat interface. However, since oblique angle of incidence makes it unclear whether the cracks reaching the interface will initiate delamination, such interactions are investigated next.

4.3. Effect of top coat cracks on TGO and top coat interface delamination

First, the TGO and top coat interface is interlaced with cohesive elements to enable simulation of delamination. The cohesive parameters are chosen ($\sigma_{\max} = 1$ GPa, $\delta_c = 1.0e-8$) such that the interface does not delaminate in the absence of the top coat crack. Fig. 8 shows an excellent agreement of the top coat stresses for perfectly bonded interface and interface laced with stiff cohesive zone. Such a stiff cohesive zone isolates the influence of top coat cracks on delamination and also represents the interface conservatively.

Next, top coat crack propagation simulations are repeated with crack trajectories reaching the interface which is laced with a stiff cohesive zone. Fig. 9 shows the eventual crack trajectories for representative geometries (a) $A = 10 \mu\text{m}$, $W = 30 \mu\text{m}$, $h = 6 \mu\text{m}$ and (b) $A = 10 \mu\text{m}$, $W = 30 \mu\text{m}$, $h = 4 \mu\text{m}$. In both cases the crack propagates along a horizontal path and intersects the interface at an oblique angle and subsequently initiates delamination extending away from undulation trough. This scenario is

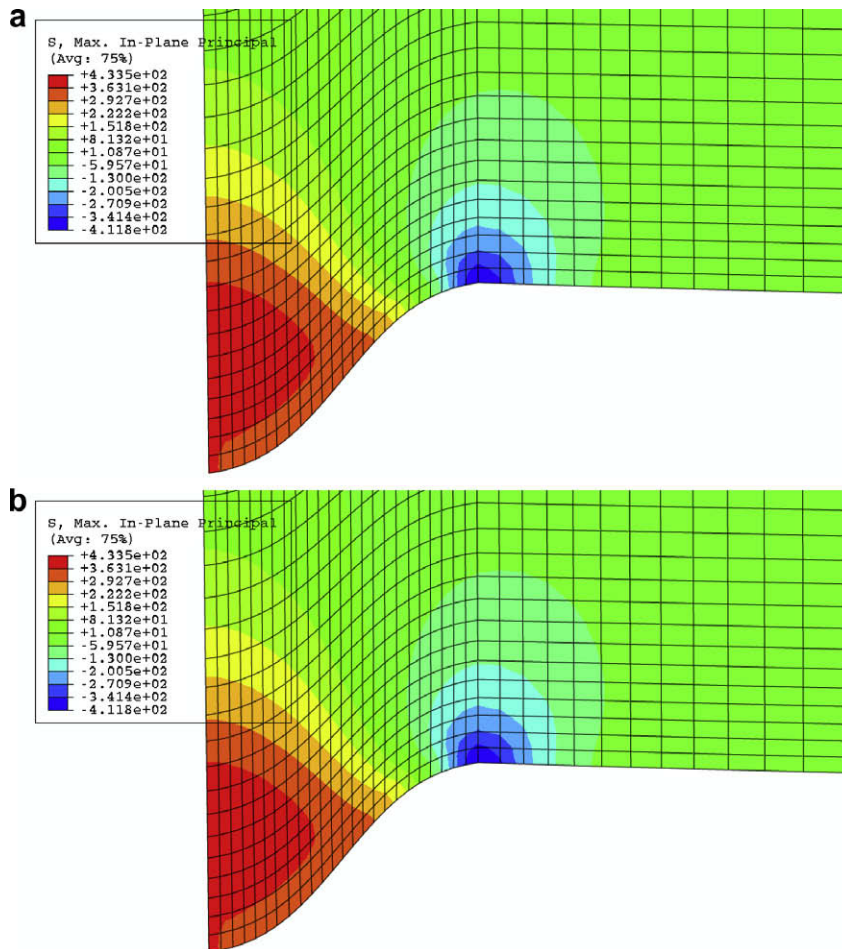


Fig. 8. Plots showing the topcoat principal stress contours when topcoat and TGO interface is (a) perfectly bonded and (b) laced with very stiff cohesive zone elements.

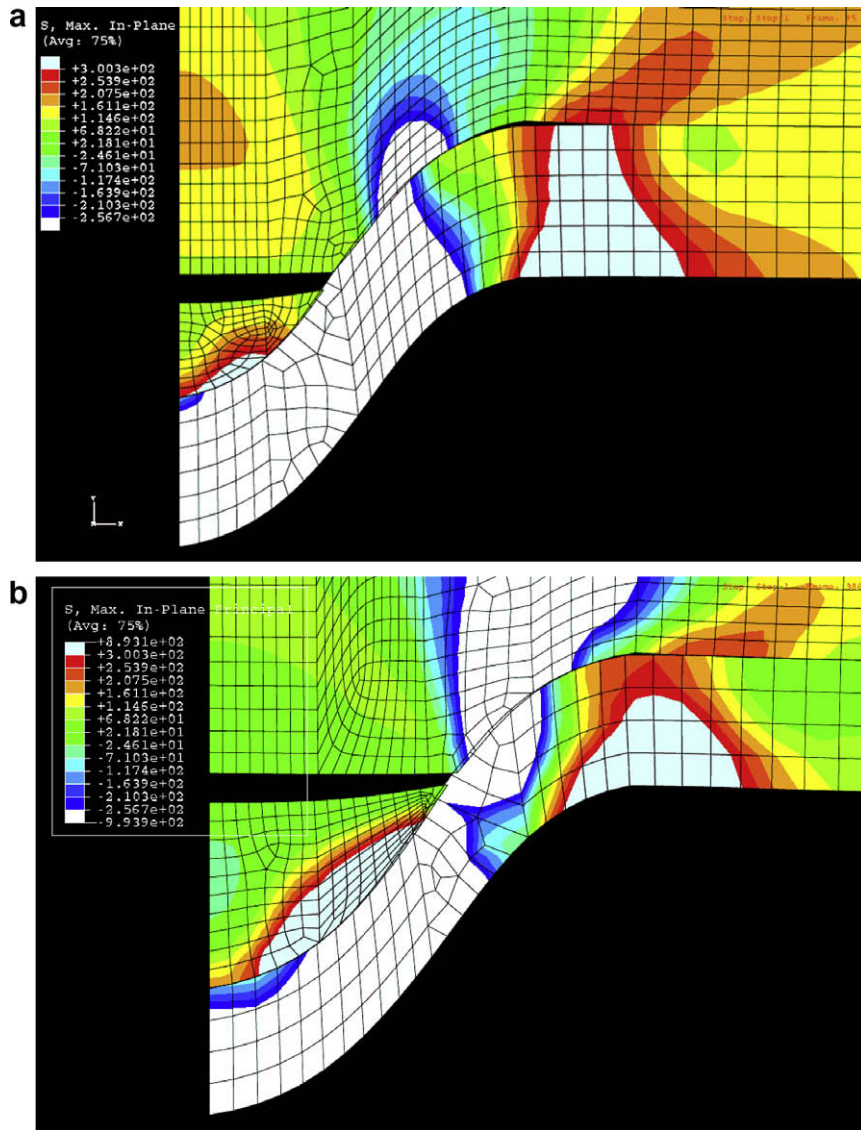


Fig. 9. Principal stress contour plots showing crack trajectories for TBC geometry defined by (a) $A = 10 \mu\text{m}$, $W = 20 \mu\text{m}$ and $h = 6 \mu\text{m}$ and (b) $A = 10 \mu\text{m}$, $W = 30 \mu\text{m}$, $h = 4 \mu\text{m}$.

typical for all crack propagation simulations and in each case the interfacial delamination extended only towards the planar interface leaving the remaining interface within the undulation intact. It should be noted that the crack propagation towards the interface is dominated by mode I, however, after reaching the interface the delamination is dominated by mode II. Hence, a change in dominant modality of crack propagation is observed as the crack intersects the interface between top coat and TGO.

5. Comparison of numerical prediction with experiments

As a final step, the predictions of finite element simulations are compared to the top coat crack trajectories ob-

served in real microstructures. Simulations are performed for TBC geometric parameters obtained from SEM micrograph in Evans et al. (2001) and nominal material parameters $E_{\text{TGO}} = 400 \text{ GPa}$, $E_{\text{TC}} = 200 \text{ GPa}$ and $\sigma_{\text{max}} = 287 \text{ MPa}$. The finite element simulation predicts that the crack initiates at a perpendicular distance of $6.38 \mu\text{m}$ from the interfacial trough and propagates to reach the TGO and top coat interface. Consequently, the interfacial delamination initiates at the site of intersection and extends towards the planar interface leaving the remaining interface within the undulation intact. This prediction closely matches the experimental observation demonstrating the capability of the proposed modeling framework to accurately predict failure scenarios. The excellent agreement between the crack trajectory observed in the SEM and finite element simulation is shown in Fig. 10.

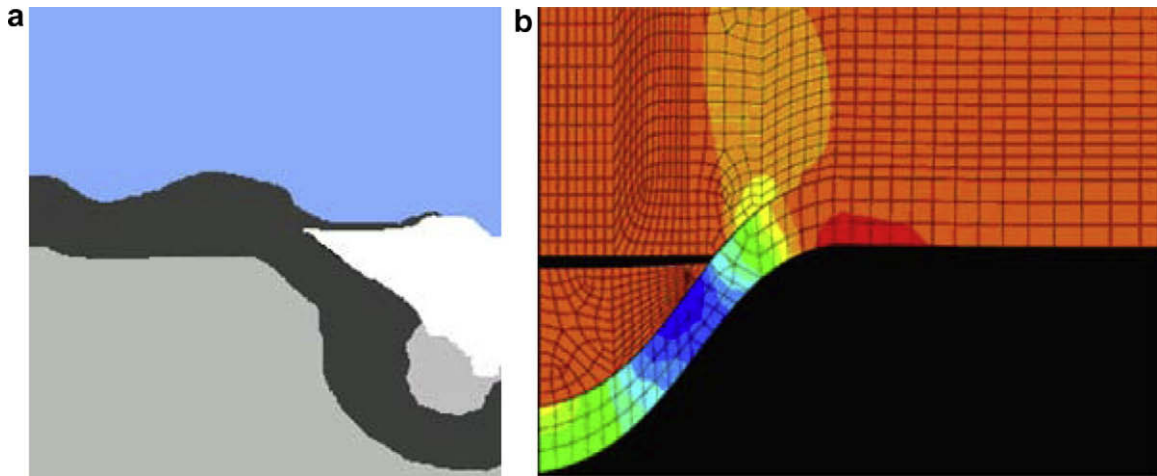


Fig. 10. Comparison of top coat crack trajectory (a) schematic of SEM micrograph observations (Evans et al., 2001) with (b) finite element simulation. The geometric parameters are $A = 10 \mu\text{m}$, $W = 30 \mu\text{m}$, $t = 3 \mu\text{m}$.

6. Conclusions

In this paper, failure of TBCs due to delaminations along susceptible interface between TGO and top coat is investigated using finite element models. The work focuses on crack initiation and propagation within the top coat that is postulated to be responsible for catastrophic failure of TBC system.

The top coat crack initiation is investigated using a thermo-elastic finite element model with bond coat creep. Crack is assumed to initiate when maximum principal stress exceeds rupture stress of the top coat. A sensitivity analysis estimates the contribution of geometric and material parameters and forms a basis to develop parametric relation to estimate maximum principal stress. The parametric relation delineates the parametric combinations that are susceptible to damage.

Subsequently, crack propagation simulations using a finite element model with embedded hysteretic cohesive zone model are performed for parametric combinations which initiate cracks away from the interface. These analyses conclude that parametric combinations initiating top coat cracks also assist in propagation and eventual delamination of TGO and top coat interface. The materials and geometries in the study are chosen to be representative of TBC materials in real applications.

The paper concludes with finite element simulations of a representative failure scenario from the literature. The geometry and material properties for this case are obtained from the literature and nominal material properties are selected for simulation. The crack trajectory predicted by simulation is found to be in good agreement with crack trajectory observed in SEM images.

Although the present study characterizes the top coat damage evolution and propagation in detail, the validity is limited to damage initiating in an idealized, defect free isotropic top coat. The top coat in real applications is anisotropic and quite heterogeneous with multiple defects (He et al., 2004). The effect of the top coat micro-structural de-

fects on the overall failure of TBCs will be investigated in a subsequent paper.

Acknowledgments

The authors are grateful for the support provided by the National Aeronautics and Space Administration (NASA) through a University Research Engineering Technology Institute (URETI) grant to the Ohio State University for Aeropropulsion and Power Technology (UAPT). Computer support by the Ohio Supercomputer Center through Grant PAS813-2 is also gratefully acknowledged.

References

- Abaqus, 2005. Users Manual. Hibbit, Karlsson and Sorrensen.
- Adams, J.W., Ruh, R., Mazdiyasi, K.S., 1997. Young's modulus, flexural strength, and fracture of yttria-stabilized zirconia versus temperature. *Journal of the American Ceramic Society* 80 (4), 903–908.
- Anderson, T.L., 1995. *Fracture Mechanics*. CRC Press, Boca Raton, FL.
- Bhatnagar, H., Ghosh, S., Walter, M.E., 2005. Parametric studies of failure mechanisms in elastic EB-PVD thermal barrier coatings using FEM. *International Journal of Solids and Structures*.
- Bhatnagar, H., Walter, M.E., Ghosh, S., 2007. A parametric domain map for top coat damage initiation and propagation in EB-PVD thermal barrier coatings. *International Journal for Multiscale Computational Engineering* 5, 227–242.
- Cheng, J., Jordan, E.H., Barber, B., Gell, M., 1998. Thermal/residual stress in an electron beam physical vapor deposited thermal barrier coating system. *Acta Materialia* 46, 5839–5850.
- Choi, S.R., Hutchinson, J.W., Evans, A.G., 1999. Delamination of multilayer thermal barrier coatings. *Mechanics of Materials* 31, 431–447.
- Evans, A.G., He, M.Y., Hutchinson, J.W., 2001. Mechanics-based scaling laws for the durability of thermal barrier coatings. *Progress in Material Science* 46, 249–271.
- Gell, M., Vaidyanathan, K., Barber, B., Cheng, J., Jordan, E., 1999. Mechanism of spallation in platinum aluminide/electron beam physical vapor-deposited thermal barrier coatings. *Metallurgical and Materials Transactions A – Physical Metallurgy and Materials Science* 30, 427–435.
- He, M.Y., Mumm, D.R., Evans, A.G., 2004. Criteria for the delamination of thermal barrier coatings: with application to thermal gradients. *Surface & Coatings Technology* 185, 184–193.
- Karlsson, A.M., Xu, T., Evans, A.G., 2002. The effect of the thermal barrier coating on the displacement instability in thermal barrier systems. *Acta Materialia* 50, 1211–1218.

- Karlsson, A.M., Hutchinson, J.W., Evans, A.G., 2003. The displacement of the thermally grown oxide in thermal barrier systems upon temperature cycling. *Materials Science and Engineering A – Structural Materials Properties Microstructure and Processing* 351, 244–257.
- Kim, H., 2005. Investigation of Critical Issues in Thermal Barrier Coating Durability. Ohio State University, Columbus, OH.
- Li, S.H., Ghosh, S., 2006a. Extended Voronoi cell finite element model for multiple cohesive crack propagation in brittle materials. *International Journal for Numerical Methods in Engineering* 65, 1028–1067.
- Li, S.H., Ghosh, S., 2006b. Multiple cohesive crack growth in brittle materials by the extended Voronoi cell finite element model. *International Journal of Fracture* 141, 373–393.
- Maiti, S., Geubelle, P.H., 2005. A cohesive model for fatigue failure of polymers. *Engineering Fracture Mechanics* 72, 691–708.
- Mumm, D.R., Evans, A.G., Spitsberg, I.T., 2001. Characterization of a cyclic displacement instability for a thermally grown oxide in a thermal barrier system. *Acta Materialia* 49, 2329–2340.
- Nguyen, O., Repetto, E.A., Ortiz, M., Radovitzky, R.A., 2001. A cohesive model of fatigue crack growth. *International Journal of Fracture* 110, 351–369.
- Ortiz, M., Pandolfi, A., 1999. Finite-deformation irreversible cohesive elements for three-dimensional crack-propagation analysis. *International Journal for Numerical Methods in Engineering* 44, 1267–1282.
- Pan, D., Chen, M.W., Wright, P.K., Hemker, K.J., 2003. Evolution of a diffusion aluminide bond coat for thermal barrier coatings during thermal cycling. *Acta Materialia* 51, 2205–2217.
- Raghavan, P., Ghosh, S., 2005. A continuum damage mechanics model for unidirectional composites undergoing interfacial debonding. *Mechanics of Materials* 37, 955–979.
- Spitsberg, I.T., Mumm, D.R., Evans, A.G., 2005. On the failure mechanisms of thermal barrier coatings with diffusion aluminide bond coatings. *Materials Science and Engineering A – Structural Materials Properties Microstructure and Processing* 394, 176–191.
- Swaminathan, S., Pagano, N.J., Ghosh, S., 2006. Analysis of interfacial debonding in three-dimensional composite microstructures. *Journal of Engineering Materials and Technology – Transactions of the ASME* 128, 96–106.
- Tolpygo, V.K., Clarke, D.R., 2000. Surface rumpling of a (Ni, Pt)Al bond coat induced by cyclic oxidation. *Acta Materialia* 48, 3283–3293.
- Wang, J.S., Evans, A.G., 1998. Measurement and analysis of buckling and buckle propagation in compressed oxide layers on superalloy substrates. *Acta Materialia* 46, 4993–5005.
- Wright, P.K., Evans, A.G., 1999. Mechanisms governing the performance of thermal barrier coatings. *Current Opinions in Solid State & Material Science* 4, 255–265.
- Xu, T., He, M.Y., Evans, A.G., 2003a. A numerical assessment of the durability of thermal barrier systems that fail by ratcheting of the thermally grown oxide. *Acta Materialia* 51, 3807–3820.
- Xu, T., He, M.Y., Evans, A.G., 2003b. A numerical assessment of the propagation and coalescence of delamination cracks in thermal barrier systems. *Interface Science* 11, 349–358.